Supplementary Information (SI) for Journal of Materials Chemistry A.

Supporting Information

Cation-Driven Hydrogen Bond Dynamics in Energy Storage Hydrogel Electrolytes: Unraveling Ion-Water-Carbon Interactions

Ezz Yousef[a†], Abdallah A. Akar[a†], Abdelrahman A. M. Ismail[a], Ghada E. Khedr[b], Nageh K. Allam[a*]

[a]Energy Materials Laboratory (EML), Physics Department, School of Sciences and Engineering, The American University in Cairo, New Cairo 11835, Egypt

[b]Department of Analysis and Evaluation, Egyptian Petroleum Research Institute, Cairo 11727, Egypt

* Corresponding Author email: nageh.allam@aucegypt.edu

† Equal Contribution

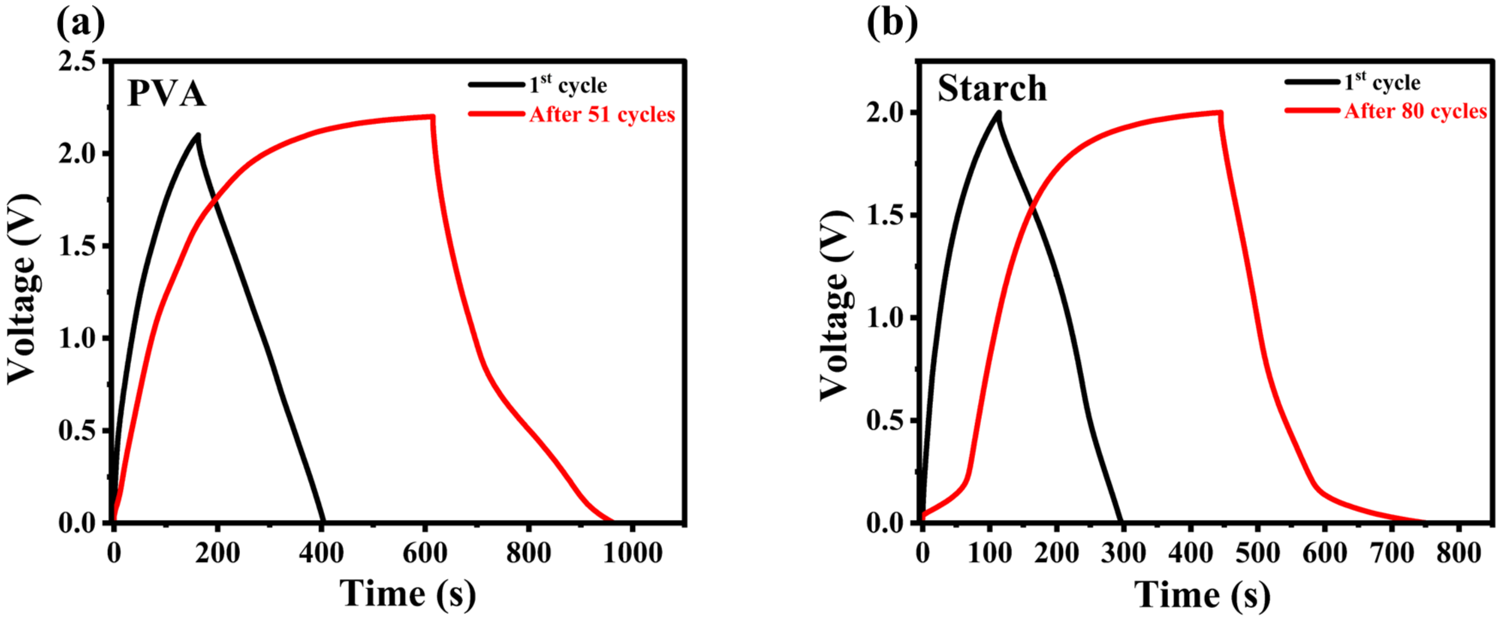

Figure S1: (a) cycle stability of CsBr@PVA, and (b) cycle stability of CsBr@starch

Table S1: The hydration sphere radius, molar ionic conductivity, and ionic radius of different cations.

Ion	Hydration sphere radius (Å)	Ref	Molar ionic conductivities in water at 298 K, λ (mS m^2 mol^{-1})	Ref	Ionic radius (Å)	Ref
Li+	3.82	[1]	3.87	[2, 3]	0.69	[4]
Na+	3.58	[1, 5]	5.01	[2, 3]	1.02	[1, 4]
K+	3.31	[1, 5]	7.35	[2, 3]	1.38	[1]
Cs+	3.1	[6]	7.72	[2, 3]	1.67	[4]

Table S2. The ionic mobility and ionic radius of different anions.

Ion	Ionic Mobility (S, Ohm^{-1}cm^{2})	Ref	Ionic radius (Å)
CH_3COOH^-	40.9	[7]	---
Cl^-	76.4	[7]	1.67
Br^-	78.1	[7]	1.96

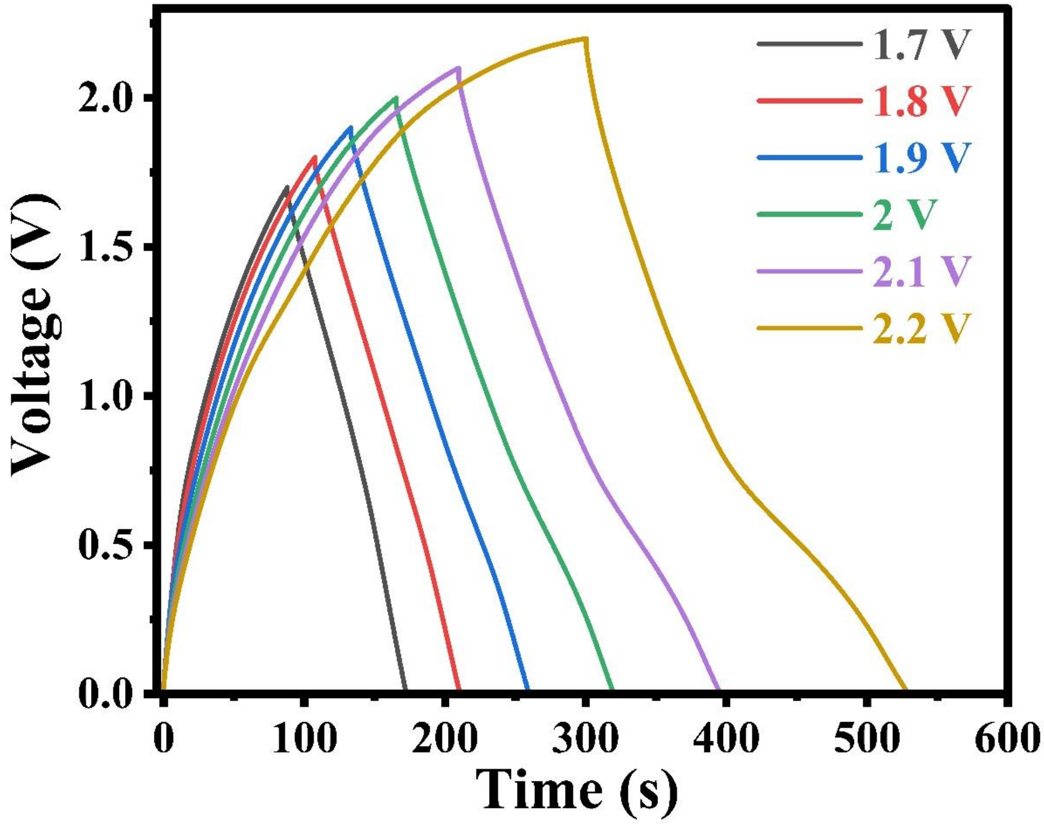

Figure S2: GCD scans at different potential windows of CsBr@PAM/HA.

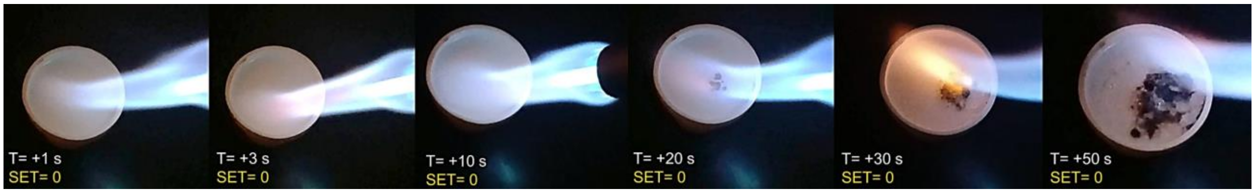

Figure S3: The flammability test for the CsBr@PAM/HA electrolyte at different irradiation time

Cesium cost

Cesium, known as the rarest of the naturally occurring alkali metals, is primarily sourced from mineral pollucite, concentrated in select locations around the world. Notably, Canada's Bernic Lake deposit has been a significant source [8]. Cesium is frequently found in liquid waste generated by nuclear power reactors and other facilities, rendering it a notable consequence of nuclear activities [9]. Significant deposits of cesium exist in Chinese salt lakes, where efficient extraction techniques are being devised to recover cesium from brines [10, 11]. Advances in solvent extraction and ion exchange technologies have significantly enhanced the feasibility and cost-effectiveness of extracting cesium from such brines, offering industrial-scale solutions adaptable to different operational needs [12]. Economic analyses have projected that the improvements in extraction methods, including the development of high-capacity ion-exchange resins, could potentially lower cesium production costs to below $2 per pound [13]. One promising method involves dissolving cesium from pollucite using sulfuric acid to produce cesium alum, requiring further purification but offering economic promise [14]. Additionally, the recycling of cesium formate, used extensively in oil drilling for its lubricating properties, exemplifies an efficient use-case scenario. With a recovery and reuse rate reaching 85%, the recycling process significantly trims costs associated with new raw material extraction [15]. Beyond traditional sources, high-level liquid waste streams from nuclear processes also provide a rich potential supply of cesium, particularly the isotope 137 Cs. Advances in the selective extraction of cesium from these streams, using specialized ion-exchange materials, promise not only to bolster supply but also to address radioactive waste management challenges efficiently [16]. Utilizing industrial byproducts and waste streams thus reduces reliance on limited pollucite reserves, unlocking new revenue streams within existing frameworks and mitigating the environmental impacts of conventional mining [11]. Diversifying cesium sources through cutting-edge recovery and recycling techniques stabilizes market dynamics and secures supply chains against geopolitical and economic flux [17]. As ongoing research continues to refine and expand cesium extraction and application, its role in technological advancements, energy, electronics, and environmental management is poised for significant growth, cementing its strategic importance in the global economy [18].

Ion transport mechanism of HCl

The charging and discharging process of a supercapacitor with HCl as the electrolyte involves the movement of H^+ and Cl^- ions, which is influenced by the polarity of the electrodes and the establishment of the electric double layer (EDL) at each electrode surface. During the charging process of the supercapacitor, the electrode linked to the positive terminal of the power source is designated as the positive electrode (anode), while the electrode connected to the negative terminal is identified as the negative electrode (cathode) [19]. Protons, which carry a positive charge and exhibit remarkable mobility due to their small size and limited hydration shell, move towards the negatively charged electrode, known as the cathode, where they gather at or near the surface of the electrode. On the other hand, Cl^- ions, possessing a negative charge, migrate towards the positively charged electrode (anode) and gather at that location. The movement and gathering of ions at the electrode interfaces create the electric double layer (EDL), which serves as the fundamental process for charge storage in electric double-layer capacitors (EDLCs). When discharged, the external circuit facilitates the flow of electrons, while the ions in the electrolyte move in the opposite direction to counterbalance the charge separation, resulting in the release of stored energy. The elevated ionic conductivity and minimal hydrated radii of H^+ and Cl^- in HCl enable swift ion mobility, enhancing the exceptional capacitance and rate performance noted in

HCl-based supercapacitors. This mechanism is thoroughly documented in existing studies and is essential for the functioning of supercapacitors utilizing aqueous electrolytes like HCl [19, 20].

Computational details:

The graphite unit cell containing 4 carbon atoms was imported from the Materials Studio 2017 library. A (4 × 4 × 2) supercell was built from the unit cell, resulting in a slab composed of 128 carbon atoms (4 layers × 32 atoms per layer). This supercell size was selected to provide sufficient surface area and to minimize lateral interactions between periodic images. A vacuum layer of 20 Å was added along the z-direction to eliminate any artificial interactions between periodic images. To simulate realistic surface-bulk behavior, the bottom three layers of the slab were fixed during geometry optimization, while the top layer and adsorbed species were allowed to fully relax. The adsorption setup involved placing Li^+, Na^+, K^+, and Cs^+ ions at physically relevant sites directly above the graphite surface to investigate their adsorption behavior. Bader charge analysis was performed to accurately evaluate the charge distribution and electron transfer between the adsorbed cations and the activated carbon surface. To determine the charge transfer, the net atomic charge is determined by subtracting the Bader charge from the ZVAL (valence charge) of the atom. The total charge associated with each atom was obtained from the Bader analysis, allowing us to determine the extent of charge transfer due to adsorption. We examined key structural descriptors of the water networks associated with each alkali metal cation (Li^+, Na^+, K^+, and Cs^+), including the cation- O(water) coordination numbers, O-O distances, and O-O-O angles among adjacent water molecules. Our analysis shows that the Li^+ cation coordinates with three water molecules, Na^+ and K^+ with four, and Cs^+ with five water molecules. These coordination differences reflect the cationic size and charge density, which also influence the hydrogen-bonding network. As summarized in Table S3, smaller cations such as Li^+ tend to preserve a compact and ordered hydration structure, whereas larger cations such as Cs$^+$ significantly disrupt the water network, leading to broader distributions of O-O distances and O-O angles. These results confirm that the size of the cation plays a crucial role in modulating the hydrogen-bonding network and the water arrangement at the activated carbon interface. The progressive increase in disorder from Li$^+$ to Cs$^+$ is evident from the broader and more variable geometrical parameters associated with Cs$^+$.

Table S3. A quantitative analysis for the bond angles and the distances for the different cations.

	Li	Na	K	Cs
Cation-O water coordination number	3	4	4	5
O-O distances	2.83 Å, 2.84 Å, 2.86 Å	2.71 Å, 2.77 Å, 2.79 Å, 2.82 Å, 2.88 Å	2.67 Å, 2.70 Å, 2.74 Å, 2.76 Å, 2.85 Å, 2.89 Å	2.68 Å, 2.71 Å, 2.75 Å, 2.79 Å, 2.83 Å, 2.86 Å, 3.01 Å
O-O-O angles	123°, 126°, 127°, 128°, 130°	108°, 119°, 123°, 126°, 130°, 136°	101°, 106°, 118°, 122°, 127°, 130°, 134°	96°, 99°, 104°, 110°, 113°, 119°, 123°, 135°, 139°
Cation-C	3.88 Å	2.51 Å	2.23 Å	2.1 Å

We employed a model consisting of four cations atoms (Li^+, Na^+, K^+, or Cs^+) placed above a carbon surface and surrounded by 24 water molecules, corresponding to a cation-water ratio of approximately 1:6. While the limited size of DFT simulation cells does not allow us to directly replicate bulk concentrations, our model was designed to capture the local solvation environment of each cation, particularly its first hydration shell. The 1:6 cation-to-water ratio is consistent with typical first-shell hydration numbers for alkali cations and is frequently used in DFT studies to represent localized interactions. This setup enables us to investigate how each cation perturbs the interfacial water structure without the need to model an entire bulk solution. Additionally, using the same number of cations and water molecules across all systems allows for a fair and controlled comparison of the structural effects induced solely by the cation identity. The number of four cations was chosen as a compromise between computational efficiency and system size, ensuring a statistically meaningful analysis while keeping the computational cost manageable for full relaxation. The 24 water molecules were selected to allow sufficient water–water interactions for hydrogen bonding yet not exceed the scale at which reliable DFT calculations could be performed.

In terms of positioning, the cations were initially placed above the carbon surface at hollow sites locations equidistant from surrounding carbon atoms. The initial vertical distance was set to 2.5 Å from the surface to allow relaxation toward the most energetically favorable adsorption site. The 24 water molecules were randomly packed above the cations, and water molecules distant from the cations were manually removed, retaining only the nearest 24 molecules to reflect a realistic hydration environment. Care was taken to avoid unphysical overlaps or excessively close contacts. This semi-random initial network was designed to let the DFT optimization process naturally evolve the system toward the lowest-energy hydrogen-bonding network and hydration shell structure. During geometry optimization, no positional constraints were applied to the ions, allowing them to relax freely. As a result, the final cation-surface distances varied with cation size, yielding relaxed distances of 3.88 Å, 2.51 Å, 2.23 Å, and 2.10 Å for Li^+, Na^+, K^+, and Cs^+, respectively.

References

1. J. Zhu, Y. Xu, J. Wang, J. Lin, X. Sun, S. Mao, The effect of various electrolyte cations on electrochemical performance of polypyrrole/RGO based supercapacitors, Phys Chem Chem Phys 17(43) (2015) 28666-73. https://doi.org/10.1039/c5cp04080a.
2. D.R. Lide, CRC handbook of chemistry and physics, CRC press2004.
3. P.W. Atkins, J. De Paula, J. Keeler, Atkins' physical chemistry, Oxford university press2023.
4. V.I. Volkov, A.V. Chernyak, I.A. Avilova, N.A. Slesarenko, D.L. Melnikova, V.D. Skirda, Molecular and Ionic Diffusion in Ion Exchange Membranes and Biological Systems (Cells and Proteins) Studied by NMR, Membranes 11(6) (2021) 385. https://doi.org/10.3390/membranes11060385.
5. J.R. Varcoe, P. Atanassov, D.R. Dekel, A.M. Herring, M.A. Hickner, P.A. Kohl, A.R. Kucernak, W.E. Mustain, K. Nijmeijer, K. Scott, Anion-exchange membranes in electrochemical energy systems, Energy & environmental science 7(10) (2014) 3135-3191.
6. D.Z. Caralampio, J.M. Martínez, R.R. Pappalardo, E.S. Marcos, The hydration structure of the heavy-alkalines Rb+ and Cs+ through molecular dynamics and X-ray absorption spectroscopy: surface clusters and eccentricity, Physical Chemistry Chemical Physics 19(42) (2017) 28993-29004.
7. N. Jaffrezic-Renault, S.V. Dzyadevych, Conductometric Microbiosensors for Environmental Monitoring, Sensors (Basel) 8(4) (2008) 2569-2588. https://doi.org/10.3390/s8042569.

8. L. Gao, G. Ma, Y. Zheng, Y. Tang, G. Xie, J. Yu, B. Liu, J. Duan, Research trends on separation and extraction of rare alkali metal from salt lake brine: rubidium and cesium, Solvent Extraction and Ion Exchange 38(7) (2020) 753-776.
9. N.A. Awang, W.N.W. Salleh, M.F.M. Alisah, A.F. Ismail, N. Rosman, N. Yusof, Adsorption of cesium from aqueous solution using chitosan beads, Jurnal Teknologi 81(2) (2019).
10. F.-P. Chen, G.-P. Jin, S.-Y. Peng, X.-D. Liu, J.-J. Tian, Recovery of cesium from residual salt lake brine in Qarham playa of Qaidam Basin with prussian blue functionalized graphene/carbon fibers composite, Colloids and Surfaces A: Physicochemical and Engineering Aspects 509 (2016) 359-366.
11. S. Chen, Y. Dong, H. Wang, J. Sun, J. Wang, S. Zhang, H. Dong, Highly efficient and selective cesium recovery from natural brine resources using mesoporous Prussian blue analogs synthesized by ionic liquid-assisted strategy, Resources, Conservation and Recycling 186 (2022) 106542.
12. Z. Shi, X. Du, S. Wang, Y. Guo, T. Deng, Application status of rubidium, cesium and research situation of its separation from brine with solvent extraction, IOP Publishing, p. 012081.
13. K.C. Dean, I.L. Nichols, B.H. Clemmons, III. Cesium extractive metallurgy Ore to metal, JOM 18 (1966) 1198-1202.
14. K. Patra, B. Sadhu, A. Sengupta, C.B. Patil, R.K. Mishra, C.P. Kaushik, Achieving highly efficient and selective cesium extraction using 1, 3-di-octyloxycalix [4] arene-crown-6 in n-octanol based solvent system: experimental and DFT investigation, RSC advances 11(35) (2021) 21323-21331.
15. J. Wang, S. Zhuang, Removal of cesium ions from aqueous solutions using various separation technologies, Reviews in Environmental Science and Bio/Technology 18 (2019) 231-269.
16. J.-H. Tang, J.-C. Jin, W.-A. Li, X. Zeng, W. Ma, J.-L. Li, T.-T. Lv, Y.-C. Peng, M.-L. Feng, X.-Y. Huang, Highly selective cesium (I) capture under acidic conditions by a layered sulfide, Nature Communications 13(1) (2022) 658.
17. X. Zhang, W. Zhao, Y. Zhang, V. Jegatheesan, A review of resource recovery from seawater desalination brine, Reviews in Environmental Science and Bio/Technology 20 (2021) 333-361.

18. J. He, L. Mao, X. Ma, J. Hua, Z. Cui, B. He, H. Pei, J. Li, Highly-Efficient adsorptive separation of Cs^+ from aqueous solutions by porous polyimide membrane containing Dibenzo-18-Crown-6, Separation and Purification Technology 299 (2022) 121757.
19. B. Pal, S. Yang, S. Ramesh, V. Thangadurai, R. Jose, Electrolyte selection for supercapacitive devices: a critical review, Nanoscale advances 1(10) (2019) 3807-3835.
20. D. Essam, A.M. Ahmed, A.A. Abdel-Khaliek, M. Shaban, M. Rabia, One pot synthesis of poly m-toluidine incorporated silver and silver oxide nanocomposite as a promising electrode for supercapacitor devices, Scientific Reports 15(1) (2025) 2698.